DEVELOPMENTS IN VOLCANOLOGY 3

EXPLOSIVE VOLCANISM

edited by

MICHAEL F. SHERIDAN

Department of Geology, Arizona State University, Tempe, Arizona, U.S.A.

and

FRANCO BARBERI

Istituto di Mineralogia e Petrologia, Universita di Pisa, Pisa, Italy

reprinted from *Journal of Volcanology and Geothermal Research,* vol. 17 (1–4)

ELSEVIER Amsterdam – Oxford – New York – Tokyo 1983

Journal of Volcanology and Geothermal Research, 17 (1983) 31—63
Elsevier Science Publishers B.V., Amsterdam — Printed in The Netherlands

MECHANISMS OF HYDROVOLCANIC PYROCLAST FORMATION: GRAIN-SIZE, SCANNING ELECTRON MICROSCOPY, AND EXPERIMENTAL STUDIES

KENNETH H. WOHLETZ

Earth and Space Division, Los Alamos National Laboratory, Los Alamos, NM 87545 (U.S.A.)

(Received September 15, 1982; revised and accepted December 20, 1982)

ABSTRACT

Wohletz, K.H., 1983. Mechanisms of hydrovolcanic pyroclast formation: grain-size, scanning electron microscopy, and experimental studies. In: M. F. Sheridan and F. Barberi (Editors), Explosive Volcanism. J. Volcanol. Geotherm. Res., 17: 31-63.

Pyroclasts produced by explosive magma/water interactions are of various sizes and shapes. Data from analysis of over 200 samples of hydrovolcanic ash are interpreted by comparison with experimentally produced ash. Grain size and scanning electron microscopy (SEM) reveal information on the formation of hydrovolcanic pyroclasts. Strombolian explosions result from limited water interaction with magma and the pyroclasts produced are dominantly centimeter-sized. With increasing water interaction, hydrovolcanism increases in explosivity to Surtseyan and Vulcanian activity. These eruptions produce millimeter- to micron-sized pyroclasts. The abundance of fine ash (<63 μm diameter) increases from 5 to over 30 percent as water interaction reaches an explosive maximum. This maximum occurs with interactions of virtually equal volumes of melt and water.

Five dominant pyroclast shape-types, determined by SEM, result from hydrovolcanic fragmentation: (1) blocky and equant; (2) vesicular and irregular with smooth surfaces; (3) moss-like and convoluted; (4) spherical or drop-like; and (5) plate-like. Types 1 and 2 dominate pyroclasts greater than 100 μm in diameter. Types 3 and 4 are typical of fine ash. Type 5 pyroclasts characterize ash less than 100 μm in diameter resulting from hydrovolcanic fragmentation after strong vesiculation.

Fragmentation mechanisms observed in experimental melt/water interactions result from vapor-film generation, expansion, and collapse. Fragments of congealed melt are products of several alternative mechanisms including stress-wave cavitation, detonation waves, and fluid instability mixing. All result in rapid heat transfer. These mechanisms can explain the five observed

0377-0273/83/$03.00

pyroclast shapes. Stress-wave fracturing (cavitation) of the melt results from high pressure and temperature gradients at the melt/water interface. Simultaneous brittle fracture and quenching produces Type 1 pyroclasts. Type 2 develops smooth fused surfaces due to turbulent mixing with water after fracture and before quenching. Fluid instabilities promote turbulent mixing of melt and water and produce fine ash. This kind of fragmentation occurs during high-energy explosions. The increased melt surface area due to fine fragmentation promotes high-efficiency heat exchange between the melt and water. Shapes of resulting pyroclasts are determined by maximum surface area (Type 3) and surface tension effects (Type 4). Type 5 pyroclasts result from nearly simultaneous vesicle burst and melt/water fragmentation.

INTRODUCTION

The modeling of pyroclastic rock formation is of prime importance, not only in consideration of the hazards of explosive volcanism, but also in understanding the role of volatiles in the chemical and physical evolution of magmas. The volatile species in this study is water and its equation of state under extreme conditions of pressure and temperature determines not only explosive energy but also affects post-eruptive alteration of pyroclastic deposits, an important aspect in the formation of many soils.

Two dominant mechanisms of pyroclast formation are generally considered important: (1) the magmatic mechanism which involves vesicle nucleation, growth, and disruption of the magma by exsolution of volatiles from the melt during its rise and decompression, and (2) the hydrovolcanic mechanism (see Sheridan and Wohletz, this volume) which operates during contact of melt with external water at or near the surface of the earth (marine, lacustrine, fluvatile, ground, or connate water).

Magmatic fragmentation has recently been reviewed and analyzed by Sparks (1978). Earlier informative considerations of bubble growth in magmas include Verhoogen (1951) who discussed the disruption of magma by bubble coalescence, McBirney and Murase (1970) who demonstrated the effect of gas pressure within bubbles exceeding the surface tension of the magma, and Bennett (1974) who discussed the role of expansion waves in a vesiculating magma.

In contrast to magmatic fragmentation which has been studied from both theoretical approaches and experimental evidence, hydrovolcanic fragmentation has been investigated largely by field observation. Hyaloclastite is the term suggested by Honnorez and Kirst (1975) for glass found with pillow basalts produced by non-explosive quenching and fracturing of basaltic glass whereas hyalotuff is used for explosive fragmentation of glass due to phreatomagmatic eruptions. Hyaloclastite may also be formed at depths greater than 500 m on seamounts where hydrostatic pressure is great enough to prevent vesiculation (McBirney, 1963). Consideration of the explosive mechanism and observation of blocky, equant glass shapes has resulted in the general conclusion that

hydrovolcanic (phreatomagmatic) ash is formed by thermal contraction and shattering of glass (von Waltershausen, 1853; Peacock, 1926; Fisher and Waters, 1969; and Heiken, 1971). This conclusion is supported by Carlisle (1963) who observed non-vesicular teardrop- and spindle-shaped hyaloclasts and experimentally produced curved splinters and pointed chips of sideromelane. Also, Honnorez and Kirst (1975) observed blocky grain shapes in blast furnace slags quenched by water.

Walker and Croasdale (1971), Heiken (1972, 1974), and Honnorez and Kirst (1975) used optical microscopy and scanning electron microscopy (SEM) to characterize hydrovolcanic ash produced in Surtseyan eruptions and submarine extrusion of pillow basalts. Heiken (1972, 1974) presented the most extensive SEM study of pyroclast shapes and found a marked difference in grain morphology between magmatic and phreatomagmatic ashes. Equant, blocky shapes and curviplanar surfaces with a paucity of vesicles resulted when fragmentation was caused by thermal contraction due to rapid chilling. Conversely, the flat, elongate, and pyramidal shapes and the drop-like shapes that Heiken (1972) described were variations due to magma chemistry and vesicle abundance.

Wohletz and Krinsley (1982) studied glassy basaltic pyroclasts and distinguished a number of textural features related to fragmentation mechanism from those caused by transport abrasion and secondary alteration. The frequency of broken planar surfaces decreases and the abundance of vesicle surfaces increases with decreasing energy of emplacement and with increasing median grain size of the deposit. This relationship is complicated, however, by transport processes which cause pyroclasts to increase in both roundness and number of small broken surfaces with increasing transport duration in pyroclastic surges. Many hydrovolcanic pyroclasts also have surfaces covered with fine adhering dust. This characterizing feature, the result of the cohesiveness of larger hydrovolcanic particles with the fine fraction contribution, however, may be confused or obscured by secondary alteration products such as the fine clay, opal, and zeolite materials of palagonite. In fact, strong alteration may completely obscure primary grain morphology. Since hydrovolcanic ash may be quickly altered because of its emplacement by steam-rich eruptions, care must be taken to distinguish between primary and alteration morphologies.

The size distributions of hydrovolcanic pyroclasts are strongly controlled by eruption energy which, in turn, determines dispersal mechanisms and resulting deposit types. Numerous published size analyses of pyroclasts have shown the relationship of particle size to mechanisms of transport and deposition. Walker (1971) demonstrated the size characteristics of flow and fall tephra by plotting the sorting coefficient versus median diameter. Later Walker (1973) showed that phreatomagmatic pyroclasts have a much higher degree of fragmentation than do magmatic ones.

An important consideration is that both the magmatic and hydrovolcanic fragmentation mechanisms may operate simultaneously during eruption. This situation is illustrated by Self and Sparks (1978) for phreatoplinian silicic eruptions in which the magma is initially disrupted by exsolution and expansion

disturbance initially fragmenting the melt and thereby increasing the contact surface area with water which, in turn, greatly increases heat-transfer rates. It is likely that both of these mechanisms operate during high-efficiency explosions. Heat transfer during superheating is still poorly understood and requires assessment of non-equilibrium thermodynamics, which may be a very important consideration in explosive heat-transfer process which occurs at rates three orders of magnitude greater than those in normal boiling (Witte et al., 1970).

The fragmentation-vaporization process has been shown experimentally to be a cyclic process of vapor film generation and collapse. The energy of this collapse is partially cycled back into the system, generating new contact surfaces so that the system is self-sustaining. The steps in this feedback process are included by models of Buchanan (1974), Board et al. (1974), and Corradini (1981b). They present the following cycle:

Stage 1. The initial contact of melt with water creates a vapor film at the interface. This stage includes the rise of magma into a zone of near surface water or water-saturated, unconsolidated materials.

Stage 2. The vapor film expands to the limit of condensation and then collapses. This expansion and collapse may occur several times until the energy of the collapse is sufficient to fragment the melt.

Stage 3. The penetration into or mixing of the collapsed film with the melt increases surface area.

Stage 4. Rapidly increasing heat transfer takes place as the water encloses melt fragments.

Stage 5. Formation of a new vapor film as water is suddenly vaporized by superheating. This new film expands and the process cycles back to stage two.

This feedback process allows a small vaporization zone to grow in size by many cycles until an explosion occurs. However, subsequent vapor collapses may be of limited strength so that only a non-chilled, heat conductive surface area is maintained. By this means a coarse, melt breccia is formed.

The expansion and collapse of a film jacket has been documented by high-speed cinematography by Nelson and Duda (1981). They and other investigators conclude that melt fragmentation by film collapse can occur by several mechanisms: (1) Axisymmetric collapse produces a water jet which penetrates and fragments the melt. (2) Symmetric or asymmetric film collapse allows the water to impact the melt surface. This impact generates a stress wave that is of sufficient energy to cavitate the melt. Kazimi (1976) showed that stress waves can also be formed by the violent film expand/collapse oscillation. (3) Trigger-induced film collapse causes liquid-liquid contact between water and melt which, in turn, causes rapid fuel fragmentation by Taylor instabilities. The rapid high-presure steam generation then causes further melt framentation. (4) Instability fragmentation due to the relative velocities of the melt and water occurs due to the passage of a shock wave. Both Rayleigh-Taylor and Kelvin-Helmholtz fluid instabilities develop where the lighter fluid, water, is accelerated into the melt (Board et al., 1975).

In all except the last of the above fragmentation mechanisms, vapor-film collapse is required as is also the case in explaining the small-scale laboratory tests (Nelson and Buxton, 1978). Corradini (1981b) shows that the presence of either non-condensible gasses or high ambient pressures can suppress a vapor explosion. Both of these conditions are tigger-related, that is, a quick fluctuation in either may initiate film collapse and explosion. Buchanan and Dullforce (1973) describe transition boiling effects which may cause a sudden drop in heat-transfer rates and thereby trigger collapse.

The hydrovolcanic mechanism of explosive fragmentation has been noted by many workers since Fuller (1931) discussed the aqueous chilling of basalt and Jaggar (1949) wrote his detailed observations of the 1924 eruption of Kilauea Volcano. Many descriptions of the activity and resulting deposits deal with the base surge (Moore, 1967; Fisher and Walters, 1970). Sheridan and Wohletz (1981) outlined the controlling factors of hydrovolcanic eruptions using the results of field studies, laboratory analysis, and experimental investigation. Colgate and Sigurgeirsson (1973), Buchanan and Dullforce (1973), and Peckover et al. (1973a and 1973b) demonstrated the strong similarity of submarine volcanic explosions to FCIs. Although the mechanism of fuel (melt) fragmentation and controls of explosiveness are not completely understood, applications to volcanic phenomena have yielded the following conclusions (Wohletz, 1980). Explosive energy, generally expressed as a scaled quantity, is measured as the efficiency of conversion of the melt's thermal energy to mechanical energy. The mechanical energy results from flash vaporization of water due to rapid energy transfer from the melt by superheating. The mechanical energy produced is then partitioned into several dominant modes including: fragmentation energy, particle kinetic energy, seismic energy, and acoustic energies. The efficiency of this process is dominantly a function of the mass-flux ratio of melt and water into the zone of interaction and the confining pressure on that zone. Fig. 1 summarizes experimental and field studies (Wohletz and McQueen, 1981; Wohletz and Sheridan, 1982). The explosive energy curve can be subdivided into regions of Strombolian activity (mass ratios of 0 to 0.1), Surtseyan activity (ratios 0.1 to 1.00), and submarine extrusion of pillow basalt (greater than 3.00).

PYROCLASTIC SIZE ANALYSIS

A hydrovolcanic eruption consists of numerous bursts, each resulting from a water/melt interaction. The size analysis presented here assumes that individual fall and surge beds (or bedding sets) represent the deposit resulting from one eruptive burst. Samples were collected from deposits within one crater radius of the crater rim. With exception of sandwave beds, samples were taken from individual bedding layers. Single sandwave beds were found usually to be less than 1 cm thick, so samples were taken from bedding sets several centimeters in thickness. The samples were chosen to investigate the variation of size characteristics among bedforms and, therefore, the relative degree of

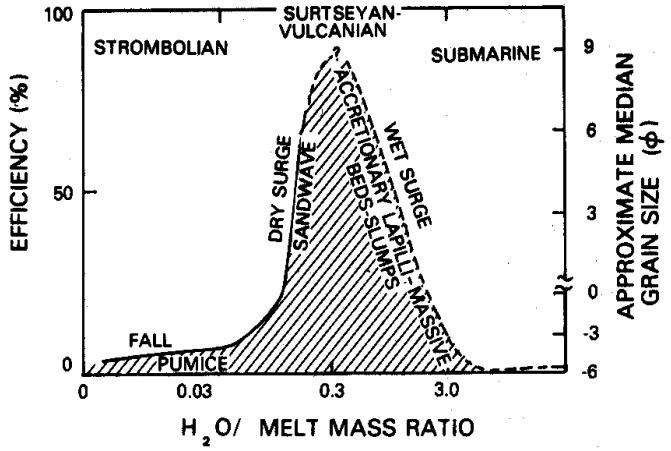

Fig. 1 Plot of conversion efficiency of thermal energy to explosive mechanical energy versus water to melt mass ratio ($\rho_{H_2O} \simeq 1.0$ g-cm^{-3}). The curve is adapted from Wohletz (1980) and also shows approximate, median grain size of melt fragments. Optimal efficiencies are expressed as percent of thermodynamic maximum. Onset of vapor explosion occurs at ratios near 0.1 and reaches a maximum near 0.3. Maximum explosive interactions produce pyroclastic surges of dry, superheated steam that deposit dune or sandwave beds. Ratios above the maximum result in wet (condensing steam) surge eruptions that deposit massive surge and flow beds. Wet surge deposits commonly are associated with accretionary lapilli, lahars, and soft-sediment bedding deformations.

fragmentation produced by each eruptive burst. This method is not strictly meaningful for fall deposits because of the strong dependence of their grain size on distance from the vent (Walker, 1971). Grain-size distributions of surge bedforms, however, do not appear to be so sensitive to distance of transport.

Figs. 2 and 3 are plots of sorting versus median diameter for 127 basaltic pyroclasts and 80 silicic samples, respectively. The plots of sandwave, massive, planar, and fall samples are delineated showing distinct fields of median size as a function of bedform. The size fields are less clearly defined for silicic pyroclasts than for basaltic pyroclasts. This result reflects upon the lower ability of high-viscosity melts to explosively mix with water. For both basaltic and silicic compositions, median sizes are: fall, 1100-2000 μm; planar surge, 750-1600 μm; massive surge, 370-650 μm; and sandwave surge, 150-300 μm.

Most size distributions of hydrovolcanic pyroclasts are polymodal. Depending upon deposit type, modes generally occur in both the coarse ash and fine ash (<63 μm) divisions which result from: (1) the degree of explosive fragmentation, and (2) subsequent sorting due to transport by inertial and viscous flow processes. Fig. 4 demonstrates the strong increase in fine ash abundance going from fall and planar surge deposits to massive and sandwave surge deposits.

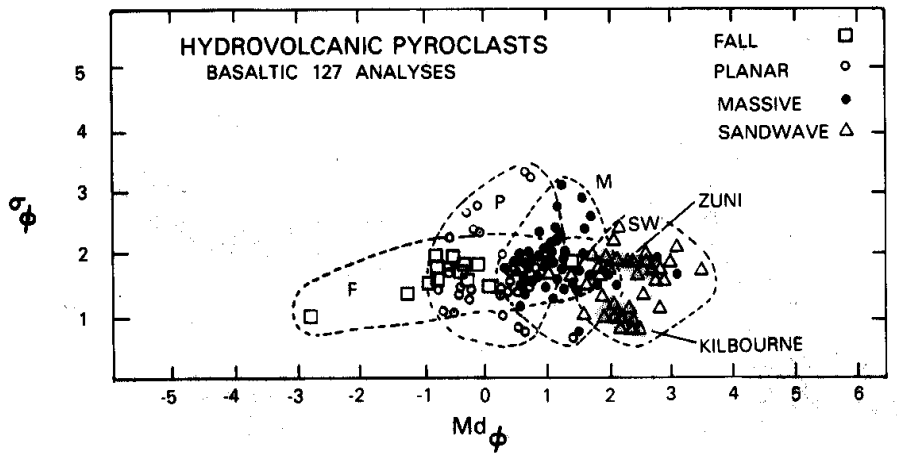

Fig. 2 Plot of standard deviation (σ_ϕ) versus median diameter (Md_ϕ, $\phi = -\log_2$ mm) for basaltic pyroclasts. Analyses of fall (F) and planar (P), massive (M), and sandwave (SW) surge deposits plot in distinct fields. Variation in sorting between sandwave deposits of Zuni Salt Lake and Kilbourne Hole result from a strong contribution of lithic (quartz sand) material at Kilbourne Hole.

SCANNING ELECTRON MICROSCOPY ANALYSIS

Following the method of Sheridan and Marshall (1982), samples were inspected with a binocular microscope to distinguish glass, lithic, and crystal constituents. Samples were cleaned using dilute HCl with ultrasound and grains were mounted individually on metal stubs. Sizes investigated include the 250 to 500 µm range and a fine fraction less than 43 µm in diameter. The SEM was operated in both the secondary electron mode at 15 keV and the backscatter mode when sample charging prevented adequate imaging. Surface charging was found to be prevalent on those grains that were most altered. Highly irregular surfaces,

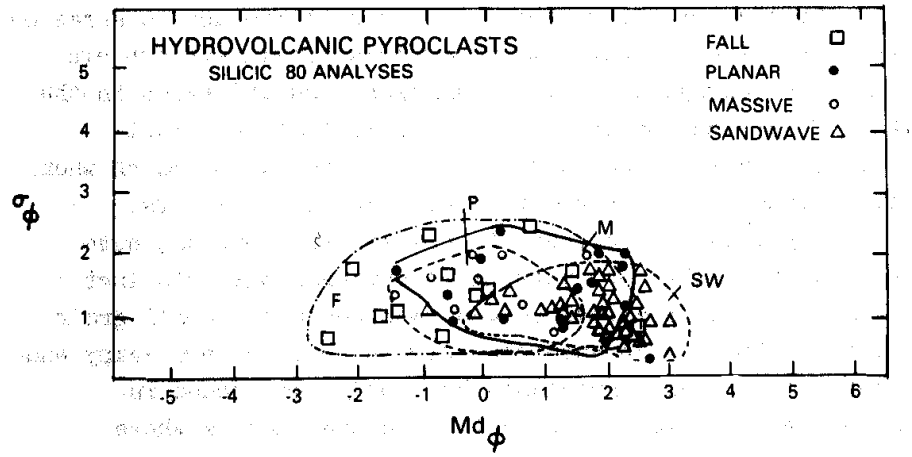

Fig. 3 Plot of standard deviation (σ_ϕ) versus median diameter (Md_ϕ) for silicic hydrovolcanic pyroclasts. Distinction of analyses of various bedforms is less apparent than for those of basaltic pyroclasts due mainly to the eruptive contribution of magmatic gasses.

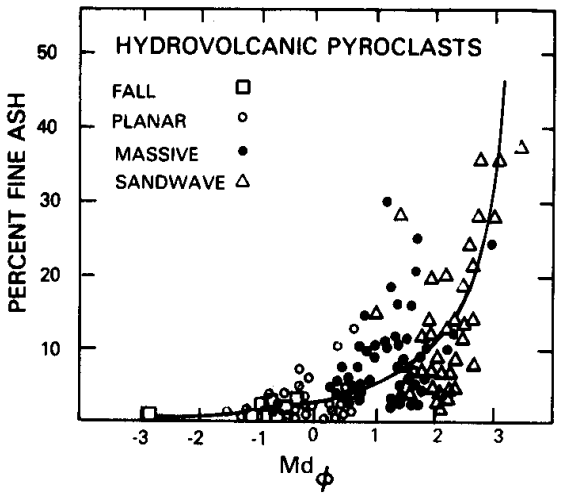

Fig. 4 Plot of percent fine ash (<63 μm diameter) versus median diameter showing an exponential increase for massive and sandwave deposits. The abundance of fine ash is a measure of explosive violence and the degree of water interaction for hydrovolcanic deposits.

prevented deposition of a uniform gold conductive coat. Altered surfaces were easily distinguished using energy dispersive spectral analysis.

Five dominant pyroclast types were distinguished from SEM images: (1) blocky, equant shapes; (2) vesicular, irregular shapes with rounded, fluid-formed surfaces; (3) moss-like, convoluted shapes; (4) spherical to drop-like shapes; and (5) platy shapes. More than one pyroclast type is commonly present in samples. However, one type generally characterizes the coarse or the fine fraction.

Type 1 pyroclasts (Fig. 5) are the most frequently observed shapes of coarse (>63-μm-diameter) hydrovolcanic ash. These "chunky" shapes are found in compositions ranging from basaltic to rhyolitic. Typically, vesicle surfaces are rare and are cut by curviplanar fracture surfaces. The equant, blocky surfaces are smooth and surface irregularities where present are due to abrasion and alteration features, or vesicle embayments. Surfaces of silicic ash are commonly slab-like. They are elongated in two dimensions and shortened in the other due to a foliation formed during injection prior to fragmentation. Pyramidal shapes are also typical expressions of Type 1 pyroclasts, which when elongated in one or two dimensions, resemble pointed chips or splinters.

Type 2 pyroclasts (Fig. 6) also are evident in coarse fractions and have surfaces controlled by vesicle walls. Flat breakage surfaces with distinct corners are absent. Vesicle edges are rounded and smoothed and overall grain shape is irregular. The smooth, curved surfaces between vesicles are lumpy and appear fused and fluid-formed. These pyroclasts have only been found in basaltic compositions and are especially abundant in Surtsey tephra where copious amounts of water had access to the vent as evidenced by periodic eruptions of water-pyroclast slurries (Thorarinson, 1966).

Type 3 pyroclasts (Fig. 7) are found only in the fine fraction (<63 μm diameter) of basalts. These moss-like, convoluted shapes have highly irregular

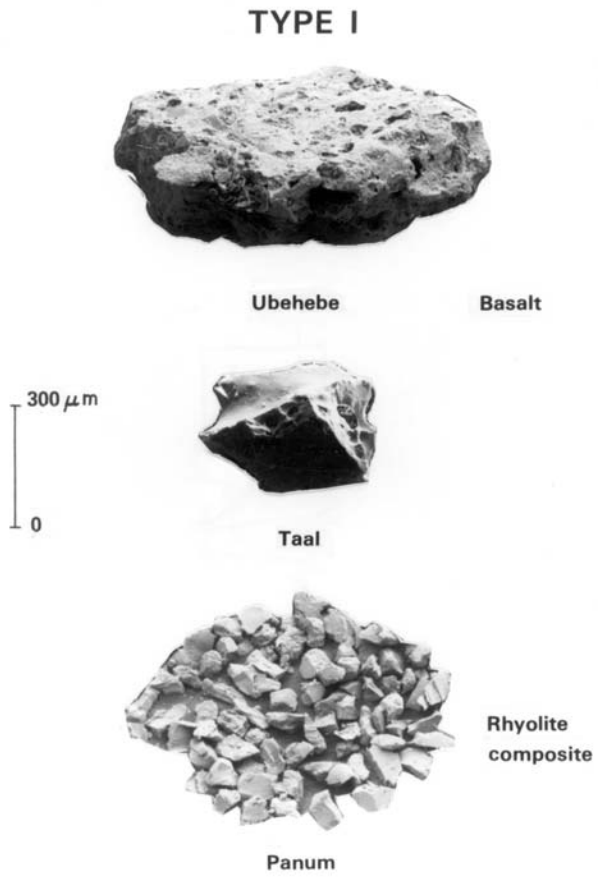

Fig. 5 SEM photomicrographs of Type I pyroclasts showing blocky shapes with curviplanar surfaces.

surfaces formed by several or more globular masses attached together. The appearance of vesicle-like embayments is due to the tortuous convolution of the composite surface, which shows smaller attached globules. The overall appearance of grains is that of delicate, interconnected structures. Some grains of this type show fluid-form connections between larger masses. The high surface area and delicate shape resembles moss.

Type 4 pyroclasts (Fig. 8) also are found in the fine fraction of basalts. This type shows roughly spherical or drop-like boundaries with smooth, curved surfaces. These pyroclasts rarely exist as separate particles. They are attached to larger blocky grains or are agglutinated to form botryoidal surface encrustations. Drop-like forms are elongated and may be broken showing vesicular interiors.

Type 5 pyroclasts (Fig. 9) include plate-like or crescent shapes. Surfaces are smoothly curved or irregular, the latter formed in magma with abundant microlites. These shapes show at least one curved surface that formed a wall of a vesicle bubble whose diameter was greater than that of the grain. This type is typical of the fine fraction of vesicular magmas. Chips and splinters of bubble walls have characteristic sharp edges.

Since hydrovolcanic pyroclasts show a multitude of grain shapes, the five types discussed above were chosen as useful divisions to characterize shapes that grade from one into another. It is likely that further investigation of

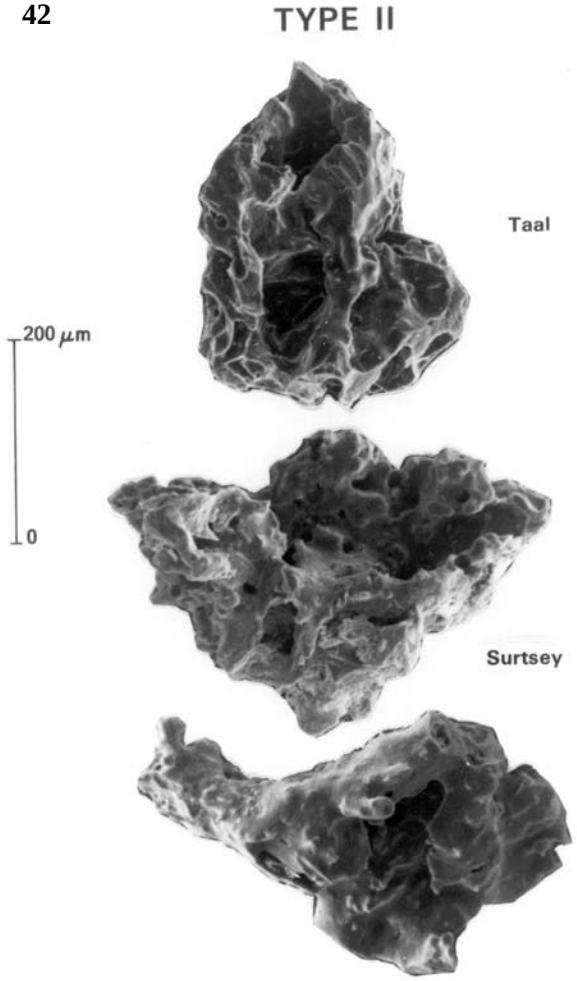

Fig. 6 SEM photomicrographs of Type II pyroclasts showing vesicular, irregular shapes with smooth, fluid-form surfaces.

magmas with unusual compositions and crystallinities will show that more types can be delineated. Many of the shapes characteristic of the fine fraction require a high-resolution stage which permits clear images of magnification in excess of 50,000 times. Samples containing pyroclasts less than a few microns in diameter have revealed quite a different spectrum of shapes (included in Types 3 and 4) than those observed in coarser ash.

EXPERIMENTAL RESULTS

The experimental basis for hydrovolcanic (water/melt) theory is from work performed over the last seven years at Los Alamos National Laboratory. The experimental apparatus and methodology are discussed in detail by Wohletz (1980), and Wohletz and McQueen (1981, in press). Concurrently and independently, research at Sandia National Laboratories by Corradini (1981a), Buxton and Benedict (1979), and Nelson and Duda (1981) investigated nuclear reactor core melt down. In both studies, the molten material used was thermite (iron oxide and aluminum).

Quartzo-feldspathic sand added to thermite in my volcano experiments produced a silicate melt approximating basaltic compositions, density, viscosity, and

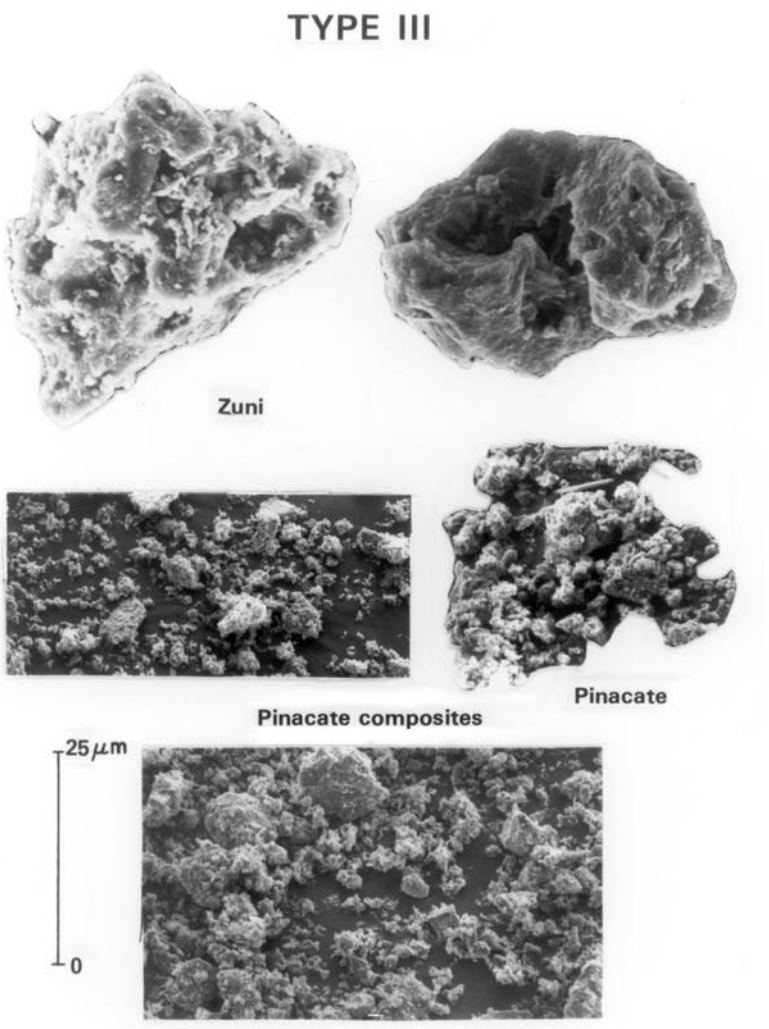

Fig. 7 SEM photomicrographs of Type III pyroclasts showing high surface-area, moss-like shapes.

phase relations. This melt was brought into contact with water inside a confinement chamber with monitoring of pressure and temperature. Venting of the chamber upon explosion was documented by high-speed cine cameras.

Variation of experimental design, melt/water contact geometry, water-to-melt mass ratio, and confinement pressure has made possible the investigation of a wide variation of explosive energy. Highly explosive experiments produced fine-grained ejected debris less than 50 μm in median diameter and less explosive interactions resulted in centimeter-sized debris. Although recovery of explosion debris is difficult because of its relatively wide dispersal away from the experimental device, size as well as SEM studies of the debris has aided in understanding the melt-fragmentation mechanism (Buxton and Benedict, 1979; Corradini, 1981a). High-speed cinematography of molten metal dropped into water (Nelson et al., 1980) also aided in the understanding of the fragmentation mechanism. The experimental debris investigated by SEM in this study shows many similarities to hydrovolcanic ash and is described below.

The experimental fallout debris was collected on polyethylene sheets. Additional debris from directed blasts was trapped using metal blocks set on the

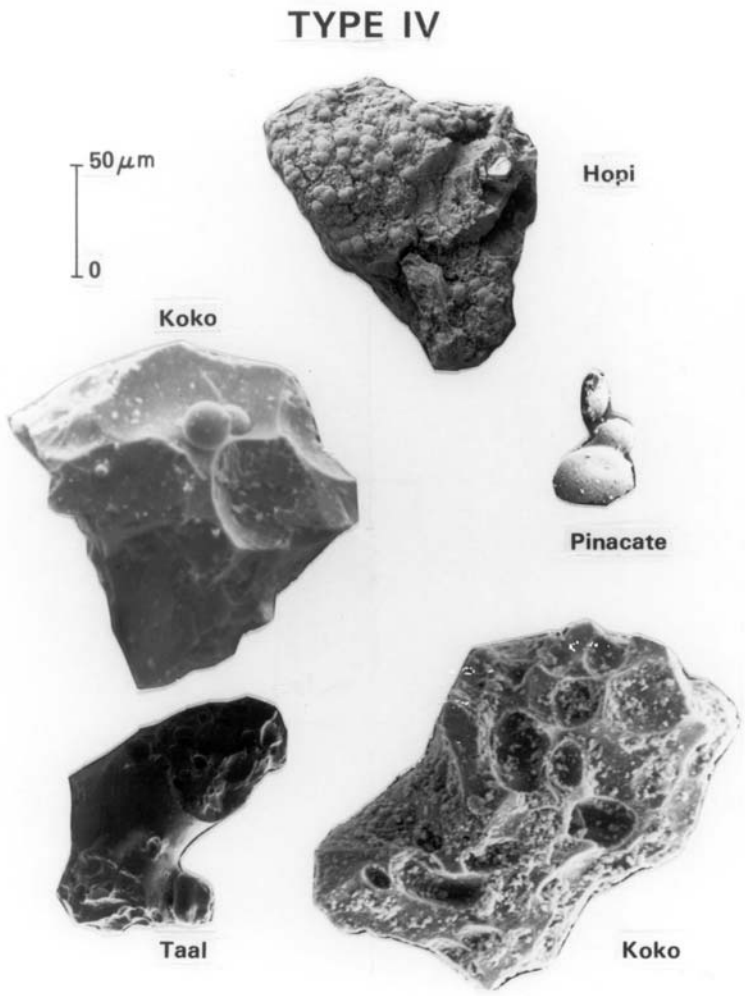

Fig. 8 SEM photomicrographs of Type IV pyroclasts showing spherical particles and drop-like shape both unattached and attached to larger particles.

sheets which served as barriers to the ejecta as it moved horizontally from the confinement chamber. Debris recovered by these means ranged in particle diameter of less than one micron to a maximum of nearly one centimeter and most was less than 50 μm in diameter.

Fig. 10 consists of micrographs of the dominant form of artifically formed explosion debris. These shapes are characterized by "moss-like" convolute shapes showing high surface area. Most surfaces are smooth and rounded forming globules and "chunks" fused together into particles usually less than 20 μm in maximum dimension. Deep embayments separate globular lobes and tiny spheres are attached on some particles. Jagged edges are rare except where ribbon-like or spongy material forms the particle lobes.

Less abundant particles have spheroidal and drop-like shapes (Fig. 11) ranging from nearly 20 to 150 μm in long dimension. Spheres commonly have smaller attached chunky and spheroidal debris. Sphere surfaces are smooth, but show intricate internal patterns of interlocking plates and elongate crystals reminiscent of Widmänstätten texture. Spheres may be attached to other debris but usually occur as separate particles. Some spheres appear to be partially

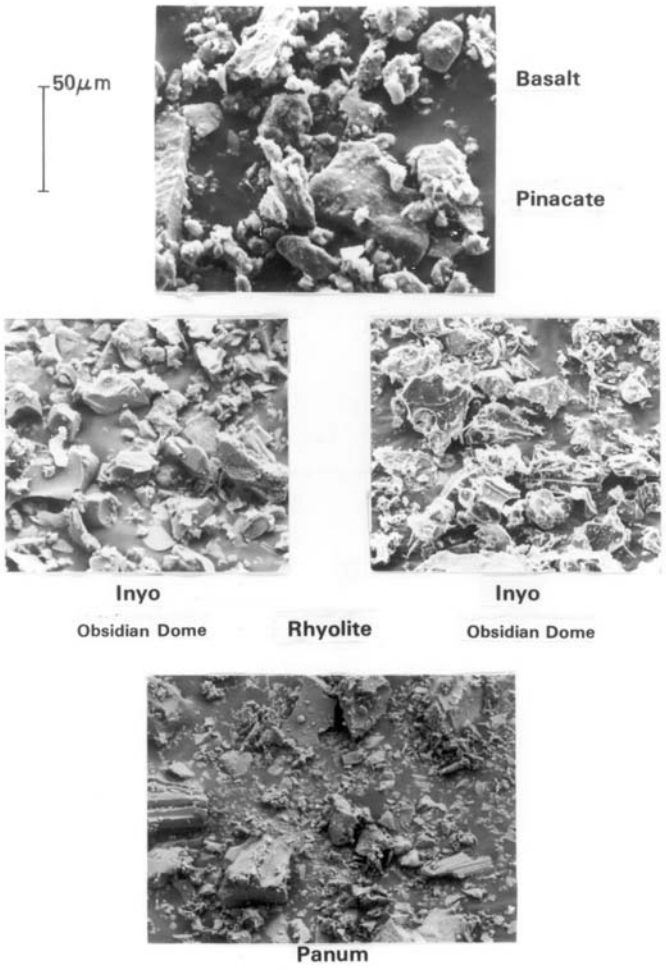

Fig. 9 SEM photomicrograph of Type V pyroclasts showing plate-like shapes and curved bubble wall shards.

hollow and have openings on their surface which reveal chunky debris inside. Drop-like shapes are usually elongated spindles with smooth surfaces and attached chunky debris.

The largest type of experimental debris shows blocky, equant shapes (Fig. 12) ranging in size from 40 to 200 μm in long dimension. Most surfaces are smooth and curviplanar; however, some show pitting and small attached particles. These forms, which show the most similarity to coarse hydrovolcanic pyroclasts, are relatively rare.

Plate-like shapes (Fig. 13) are broken pieces of curved bubble walls and angular flat chips. Although vesicles are rare in the fine experimental debris, they are common in the centimeter-sized ejecta (Fig. 14) which bears strong resemblence to basalt scoria. Gasses trapped in the thermite melt form vesicles of 0.1 to 1.0 cm in diameter.

Although thermite melt varies considerably in chemical composition from basaltic melts, its similar viscosity, density, and surface tension make it a reasonable model. Table 2 gives representative energy dispersive spectral analysis (EDS) of several melt particles. Due to incomplete mixing of the reactants during melting, the products show variation in chemistry on a fine

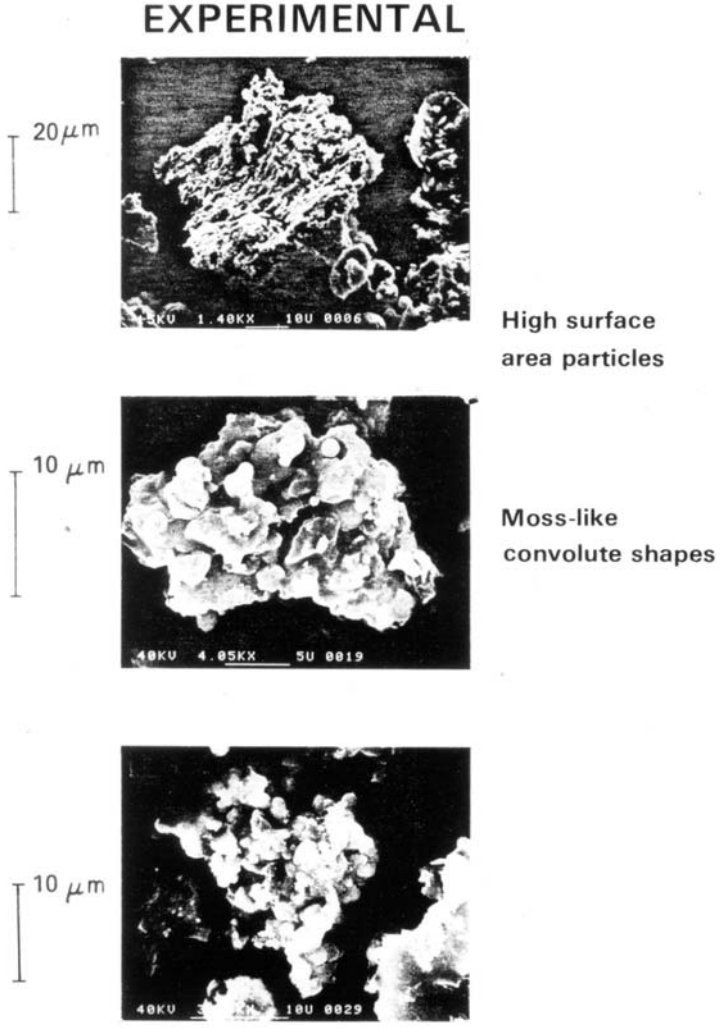

Fig. 10 SEM photomicrographs of experimental debris. These particles are typical of high surface-area convolute shapes that dominate most samples.

scale. In this section the thermite explosive product consists of thin, lath-like crystals enclosed in a quenched groundmass. The crystals are birefringent and the quenched groundmass is opaque in plane polarized light. The texture is microcrystalline variolitic.

DISCUSSION OF FRAGMENTATION MECHANISMS

Experimentally produced ash shows a strong similarity in size and shape when compared to hydrovolcanic ash. Considering the limitations imposed due to scaling and differences in bulk chemistry of the thermite from that of basalt, the following discussion of pyroclast formation illustrates the significance of size and shape.

Pyroclast Size

The dominant form of heat transfer from the melt to the water in melt/water interaction is assumed to be conductive. The difference in temperature and the contact surface area between the melt and water are important parameters in determining the rate of heat transfer and the explosive efficiency. From

EXPERIMENTAL

Fe-Al sphere

Al-Fe sphere

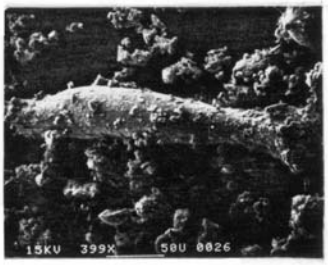

Drop-like

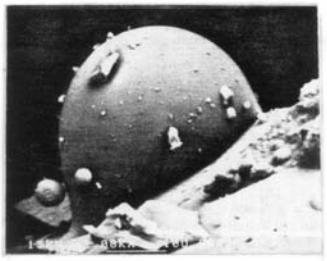

Al-Si sphere

Fig. 11 SEM photomicrographs of experimental spherical and drop-like particles. Notice the intricate pattern of crystal growth on the upper sphere and the hollow center on the sphere pictured left center.

small-scale experiments, Buxton and Benedict (1979) have quantitatively shown the decreasing fragment size with increasing explosive efficiency of thermite and water. Large-scale experiments (Wohletz and McQueen, in press) have qualitatively shown that highly explosive "Surtseyan" interactions result in micron-size fragmentation and surge dispersal of the melt, whereas less explosive "Strombolian" interactions produce millimeter- and centimeter-size fragments dispersed by fallout.

The size break between surge and fall ashes occurs near 1 mm which corresponds to the distance of penetration of a thermal wave into magma in less than 10^{-1} second. Fig. 15 is a plot of cooling time, t_c, and surface area of spherical pyroclasts versus grain diameter; t_c is calculated by two methods:

$$t_c = \frac{d^2}{D} \qquad (1)$$

$$t_c = \frac{d^2}{8k} \qquad (2)$$

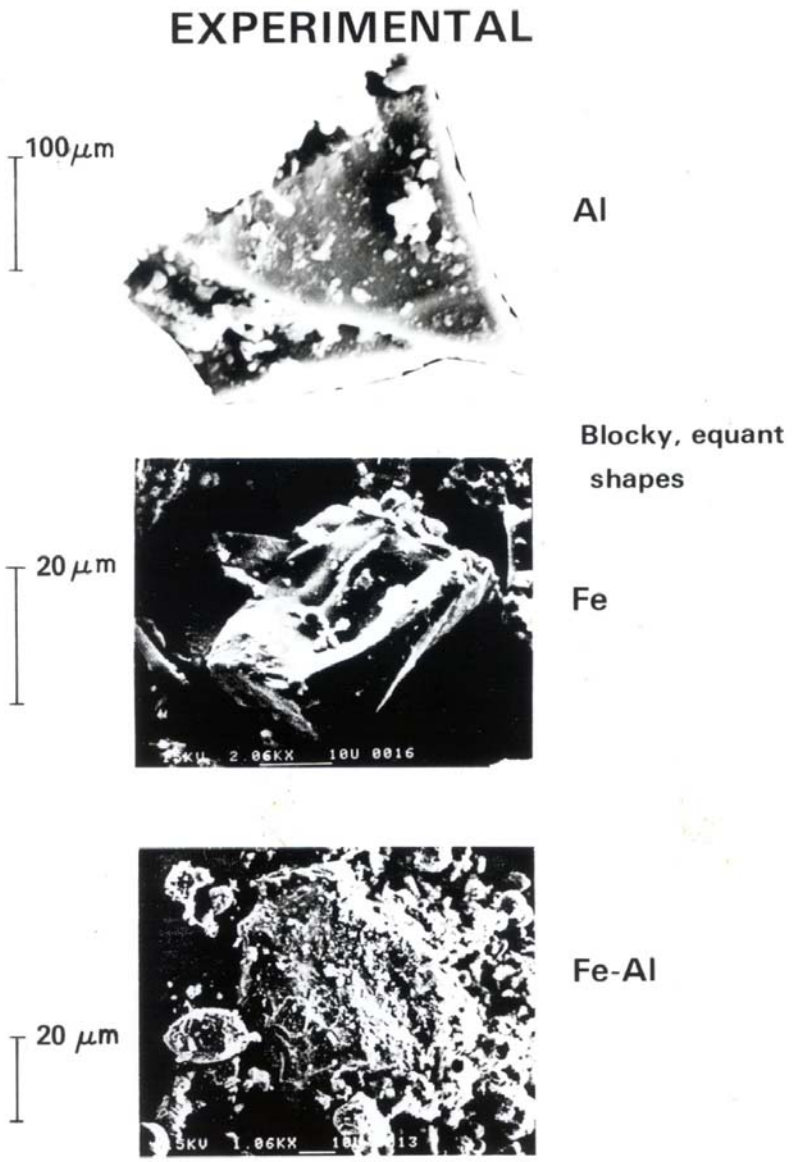

Fig. 12 SEM photomicrographs of experimental blocky or "chunky" debris. Smooth surfaces characterize most samples although some show abundant adhering fine dust.

(from Colgate and Sigurgeirsson (1973) and Sparks (1978) respectively), where d is the depth of penetration of a thermal wave (grain radius), D is the thermal conductivity, k(5×10^{-3} cal-cm^{-1}-s^{-1}-deg^{-1} for basalt) divided by the heat capacity, C_v(0.25 cal-cm^{-3}-deg^{-1} for basalt). Explosive heat-transfer times decrease over seven orders of magnitude from seconds to microseconds as grain diameter decreases from millimeters to microns. Concurrently, the specific surface area of particles increases nearly 6,000 times as melt is fragmented to micron size. The efficiency of conductive heat transfer, a function of both surface area and heat transfer time increases dramatically with increasing melt fragmentation.

Heat transfer from pyroclasts to a surrounding vapor film (Fig. 16) can be evaluated by considering heat flow from a spherical body. Integration of the conductive heat-flow equation for spherical coordinates yields Q, the rate of heat transfer expressed for unit area:

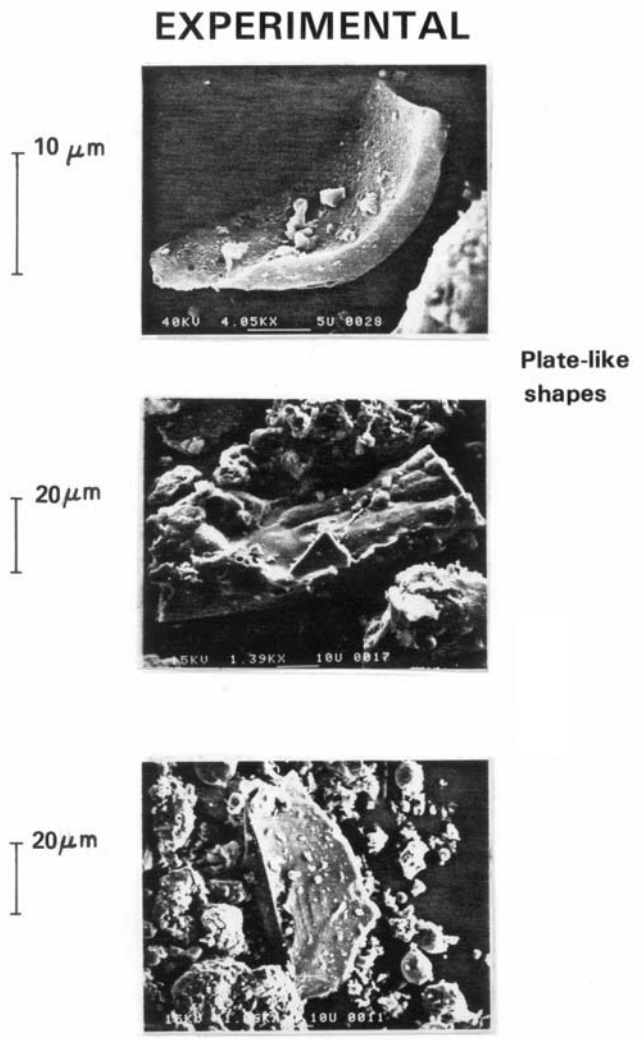

Fig. 13 SEM photomicrograph of experimental plate-like shapes. The upper photo shows a broken bubble wall that formed a vesicle from trapped gasses in the melt. Other shapes appear to have been "peeled" or cavitated as quenched skin from the surface of the melt.

$$Q = \frac{4\pi\ k(T_1 - T_2)R_1R_2}{A(R_2 - R_1)} \qquad (3)$$

where k is the conductivity of steam, R_1 and R_2 the radii of the melt sphere and the surrounding vapor film (measured from the melt sphere center) and T_1 and T_2 their respective temperatures, and A the contact area. The thermal conductivity of steam can be approximated as the linear function of temperature $6.22\times10^{-5}+2.43\times10^{-7}[T(°C)-127]$ cal-cm^{-1}-s^{-1}-deg^{-1} from values given by Weast (1977) and that of basalt is 5×10^{-3} cal-cm^{-1}-s^{-1}-deg^{-1}. Assuming a constant vapor film thickness of one tenth that of the melt sphere diameter and the temperature gradient over the film to be 20 degrees, Q increases from 6.1×10^{-2} cal-cm^{-2}-s^{-1} to 7.6×10^{2} cal-cm^{-2}-s^{-1} as the particle diameter decreases from about 1 cm to 10 μm.

Fig. 17 is a plot of data from Buxton and Benedict (1979) showing melt-fragment median diameter versus the experimental explosion efficiency. Median fragment diameters of 2 mm or greater were recovered from non-explosive

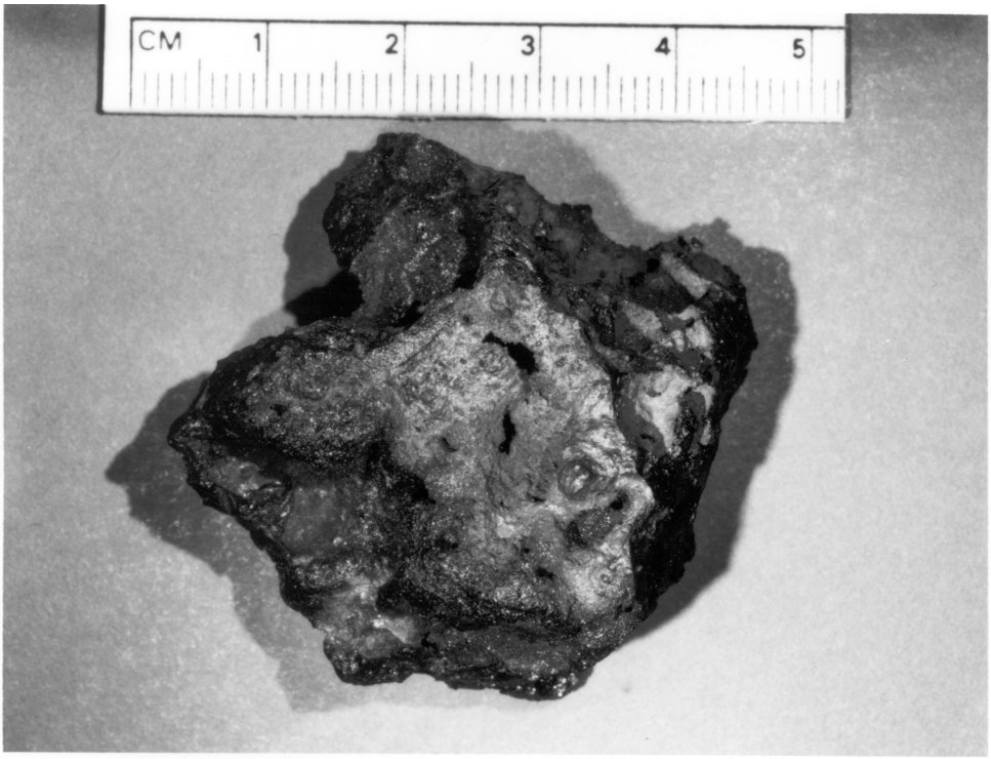

Fig. 14 Photograph of a piece of experimental scoria. The vesicles and jagged edges as well as similar density and color make this sample difficult to distinguish from basalt scoria.

TABLE 2

Representative chemical analyses* of thermite melt debris

Oxide	1+	2	3	4	5
SiO_2	10.1	10.7	14.3	36.6	18.6
TiO_2	-	-	2.3	1.4	1.9
Al_2O_3	31.2	25.1	11.4	34.4	42.5
FeO	57.9	64.2	57.0	17.3	23.3
MgO	-	-	6.4	3.7	5.8
MnO	-	-	1.6	1.0	1.3
CaO	0.5	-	2.1	1.7	1.9
Na_2O	-	-	3.1	2.0	3.2
K_2O	0.3	-	2.0	2.0	1.9

*Standardless energy dispersive spectral analyses (EDS)
+1 - Iron-aluminum sphere, large
2 - Iron-aluminum sphere, small
3 - Blocky iron particle
4 - Coating on iron particle
5 - Iron-aluminum spindle

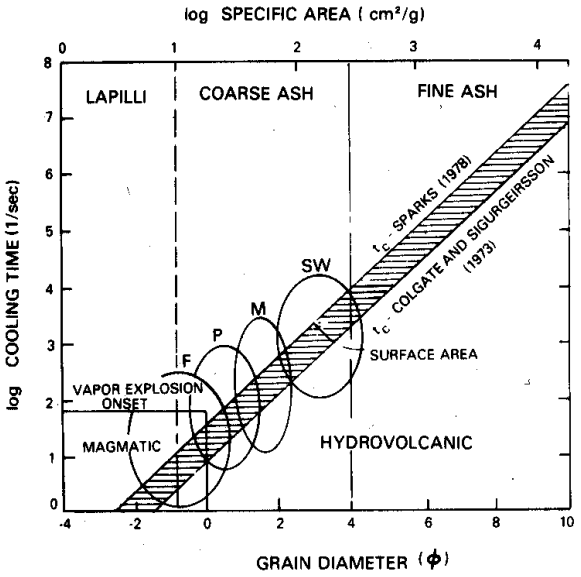

Fig. 15 Plot of penetration time of a thermal wave into a spherical pyroclast versus grain diameter. This time decreases exponentially with grain size and is calculated by the two similar formulae from Sparks (1978) and Colgate and Sigurgeirsson (1973). The specific area of grain surfaces increases exponentially with decreasing grain size. High surface area and short thermal equilibration times 10^{-1} to 10^{-2} s are required for vapor explosions. This boundary is near that for the division of lapilli and coarse ash (2 mm), and for basalts the division is between dominantly magmatic Strombolian and hydrovolcanic Surtseyan eruptions. The fields of grain size are shown for fall and surge deposits and demonstrate a two order of magnitude increase in surface area for hydrovolcanic over non-hydrovolcanic pyroclasts.

experiments. Fig. 17 also shows the calculated rate of conductive heat transfer, Q, from Eq. (3) versus fragment size, R_1, showing the range of values obtained for steam at temperatures between 300 and 1180°C heated by basaltic melt droplets at 1200°C. The surface area dependency of conductive heat flow upon fragment size demonstrates an exponential relationship of explosive efficiency to degree of fragmentation. Initial vapor expansions produce tensile stresses and fluid instabilities that increasingly fragment the melt resulting in an exponential increase in explosive, conductive heat transfer. The partitioning of vaporization energy into melt fragmentation and ejection modes is dependent upon the density, viscosity, surface tension, and yield strength of the steam and the melt, their seismic and acoustic velocities, and two phase flow complexities.

The partial effect of the steam film thickness (R_2) upon heat transfer can be derived from Eq. (3) to give a conductive factor:

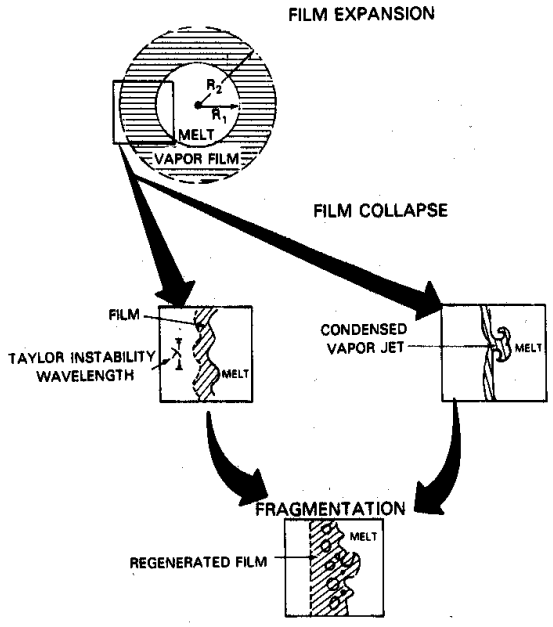

Fig. 16 Diagrammatic illustration of the film collapse model showing fragmentation during collapse by Taylor instabilities and water jetting.

$$dQ]_{R_1} = - dR_2/(R_2-R_1)^2 \quad .$$

The above equation is a hyperbolic curve with an inflection near a point where the steam film radius, R_2, is twice that of the melt sphere radius, R_1. The change in heat conductance due to the conductive factor is shown for different values of R_2 in Fig. 18. Q increases logarithmically as the steam jacket R_2 decreases in thickness below a value equal to nearly 2 to 5 times that of the thickness R_1 (the depth of the thermal wave penetration in the melt). Above this value, Q remains constant as R_2 varies. During collapse of the film jacket, Q increases to the point where the condensed phase is instantaneously vaporized forming an expanding steam jacket. During expansion, Q decreases to a minimum point where the bubble becomes unstable again and collapses.

Drumheller (1979) approaches the problem of vapor-film collapse by calculating the energy and work of vapor and liquid water surrounding molten iron spheres at 1600°C. These quantities are dominantly functions of the film and melt sphere radii, rate of condensation, and vapor densities. The functions are integrated over time to obtain the equations of motion which, when evaluated with heat conductivity requirements, predict the following: For 5- and 10-mm-diameter melt spheres, the collapsing film reaches impact velocity peaks of 3 to 7 ms^{-1} and impact pressures of 5 to 10 MPa for film thicknesses of about 0.05 to 0.1 mm. The functions expressing these values are strongly damped with increasing ambient pressure. Pressure waves generated in the melt sphere reach peak values approaching 25 MPa on microsecond time scale. These values when

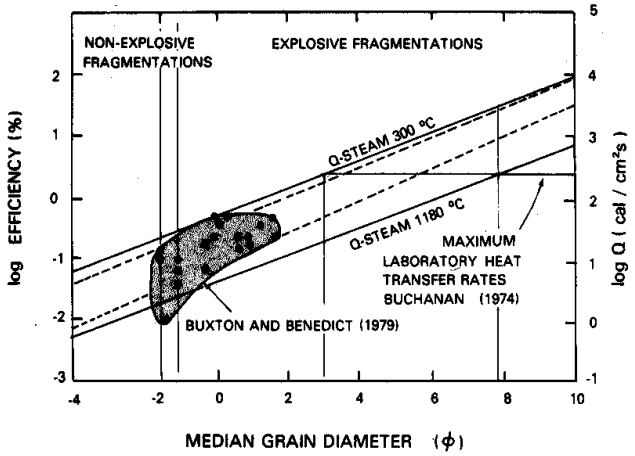

Fig. 17 Plot of conversion efficiency of thermal to mechanical energy versus median grain size of debris formed by experiments. Points shown are from medium scale (10-20 kg thermite) experiments (Buxton and Benedict, 1979) and fall on an extrapolated trend (dashed lines) that intersects maximum thermodynamic efficiency near 10 ϕ. Below -1.0 to -1.5 ϕ fragmentations of thermite due to contact with water were non-explosive. Also plotted are values of heat-transfer rates, Q, versus grain size showing an exponential increase with decreasing grain size. The maximum measured laboratory rates corresponds to fragmentation sizes between 3 ϕ (125 μm) and 8 ϕ (4 μm), which are observed in small-scale laboratory (~1 g) experiments. Values of Q are calculated for thermal gradients between basalt at 1200°C and steam at 1180°C and 300°C.

considered with surface tension effects are great enough to cause fragmentation of the melt (Galloway, 1954) thereby increasing the surface area by over two orders of magnitude.

Corradini (1981a) models FCI experiments using a thermal fragmentation mechanism. In this model near fuel-coolant contact during film collapse generates Taylor instabilities and high-pressure vapor at the contact. The instabilities fragment the melt which is subsequently quenched during convective mixing and heat transfer. This model predicts the generation of a high-pressure wave (150 MPa) propagating at 90 ms^{-1}. Critical to these calculations are those of equilibrium pressure via a Redlich-Kwong equation of state. These pressures cause acceleration of the fuel giving rise to instabilities. The Taylor wavelength, a function of film thickness, melt and vapor densities, and melt-acceleration determines the surface area increase.

Board et al. (1975) show that the structure of FCIs may produce a detonation wave. High pressures observed in laboratory experiments and fast propagation of these pressure waves suggest the development of shock waves. The front of the wave shatters the melt. Vaporization due to fuel-coolant thermal equilibrium occurs directly behind the shock front and the expanding vapors drive and

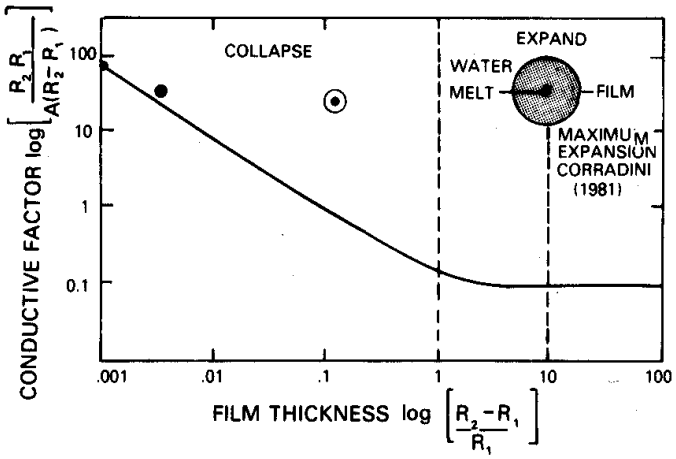

Fig. 18 Plot of a conductive factor versus vapor film thickness, R_2, normalized to a constant melt sphere radius, R_1. As the film collapses to small thicknesses, the conductive heat transfer from the melt to the film increases rapidly until an additional volume of water is vaporized. The film then expands (Corradini, 1981a) while conducting progressively less energy until heat transfer to the vapor eventually reaches a minimum. At that point heat energy is lost from the vapor to the surrounding fluid, vapor expansion slows, and condensation occurs causing the film to collapse. This process may be repeated many times on a millisecond scale. Each collapse fragments more melt resulting in larger heat transfers and greater volumes of vaporized water. The process will continue until vapor expansion is greater than confining pressure and the system explodes.

maintain the front. This mechanism is analogous to detonation of chemical explosives in which the generated gas drives the detonation wave. Board et al. (1975) calculate that pressures as high as 1.5×10^3 MPa (15 kbar) could be generated by this mechanism in large systems. The passage of the shock front also produces large velocities of the fuel relative to the coolant. These velocities are sufficient to develop both Rayleigh-Taylor and Kelvin-Helmholtz fluid instabilities which cause melt fragmentation (Theofanus, 1979; Berenson, 1961).

Shock propagation may also initiate axisymmetric vapor film collapse causing water jets to penetrate the melt. In this model, Buchanan (1974) calculates the energy of film collapse, and the penetration depth, heat transfer, and fragmentation size of the water jet. After each collapse and fragmentation, more water is vaporized and the cycle repeated. In his model, Buchanan (1974) shows that the first cycle of vapor collapse produces a film with an energy of 1.2×10^{-4} J and thickness of 6.6×10^{-4} m in 2.6×10^{-3} s. This cycle fragments a very small amount of melt (2.2×10^{-11} kg) and produces a peak pressure of 0.33 MPa. After six cycles and an elapsed time of 0.21 s, the vapor film is 1.3 m thick with collapse energy of 9.8×10^5 J. At this point 0.17 kg of melt has been fragmented and a peak pressure 662 MPa is produced by the feedback mechanism. This model also predicts a strong damping affect due to the

system ambient pressure and illustrates the remarkable efficiency of FCIs.

With these discussions in mind let us return to the problem of hydrovolcanic fragmentation. The pyroclast size-distributions of the various bedforms shown in Figs. 2 and 3 pose some difficulty for interpretation. This difficulty lies in the fact that pyroclastic deposits generally become finer grained with distance from the vent. For sandwave beds, Sheridan and Updike (1975) found median diameter to vary nearly two phi-size units with distance from the vent. This variation, however, did not show a systematic "fining" of grain size. Data given by Wohletz and Sheridan (1979) suggest that overall, the median diameter of surge tephra varies less than one phi-size unit within a given bedform at varying distances from the vent. Although this problem has not been studied systematically, the following interpretation of size data is put forth based upon models of surge eruption and emplacement. An FCI model for surge eruption predicts that the most explosive interactions produce the greatest steam-to-pyroclast volume ratio and the finest grain sizes. Using the grain-size data in Fig. 4, this model indicates a likelihood of sandwave deposition if highly explosive eruptions produce surges, which is in agreement with experimental observations (Wohletz and McQueen, 1981). Independent of the FCI model, Wohletz and Sheridan (1979) suggested that sandwave, massive, and planar bed forms are deposited from surges of decreasing void space (decreasing steam-to-pyroclast volume ratio). Assuming the validity of these models, variation of grain size among surge bedforms at near-vent localities reflects a fluctuation in the explosivity of the eruptions that produced the tephra. In this reasoning, highly explosive eruptions result in emplacement of dominantly fine-grained sandwave surge deposits while massive and planar surge deposits of coarser grain sizes are emplaced after less explosive bursts.

Pyroclast Shape

The shape of the fragments produced is complexly dependent upon the physical properties of the melt and rate of heat energy release as mentioned earlier. Fragmentation may be of a brittle, ductile, or viscous nature depending upon the viscosity, surface tension, and yield strength of the melt. Each of these deformation modes will produce a distinct fragment shape. The dominant mode of deformation, as evidenced by shape, may be related to one of the fragmentation mechanisms outlined above.

Brittle and ductile fractures depend upon the strength of the melt. Cavitation due to brittle fracture may result from stress waves propagating into the melt forming regions of tension and compression. If the strain rate exceeds the melt bulk modulus, then brittle failure will occur with increasing tendency as confining pressure decreases. Fractures will propagate at an angle less than 45° to the direction of compression or extension. This mechanism could explain the formation of blocky pyroclasts Type 1 and Type 2. Fig. 19 illustrates this model. Quenching and solidification during and after brittle fracture preserves blocky shapes with curvi-planar surfaces. More ductile behavior would result in irregular or elongated fragments. If solidification and formation of a quenched

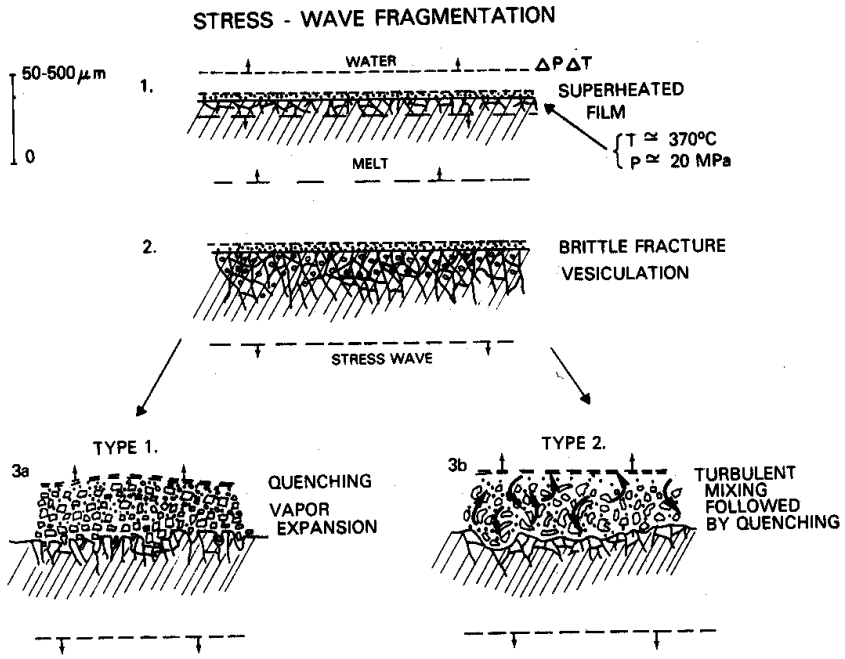

Fig. 19 The collapse of a superheated vapor film or the explosive expansion of the film will produce stress waves in the melt. If these exceed the bulk modulus of the melt and it fractures brittly, blocky Type 1 or Type 2 pyroclasts may form.

crust is not complete after fracture, subsequent movement of fragments out of the zone of interaction forms smooth, fluid-like surfaces on fragments (Type 2).

Fluid instabilities resulting from either water jet penetration of the melt or Taylor and Kelvin-Helmholtz mechanisms result in turbulent mixing of the melt and water. Viscous deformation of the melt dominates and fluid-form shapes result. Repeated vapor-film collapses generate high surface-area particles on a millisecond time scale. When heat-transfer rates due to high surface area result in vapor generation at pressures greater than the confining system pressure, vapor explosion occurs. Moss-like, Type 3 (Fig. 20) pyroclasts result from viscous effects of the melt whereas spherical or drop-like shapes, Type 4 (Fig. 21) are due to the dominance of surface tension effects. These instabilities are highly probable features at the contact of the melt and water because of the density difference between the two fluids, accelerations due to vaporization, hydrostatic head, and explosion shock waves as well as the seismic disturbances that exist in a volcano.

Type 5 pyroclasts are most typical in silicic deposits and characterize phreatoplinian eruptions (Self and Sparks, 1978). The burst of vesicle bubbles fragments the rising magma and propels shards into a zone of mixing with external water. The following rapid vaporization fractures the shards and produces stress waves in the melt that may enhance vesiculation (Bennett, 1974)

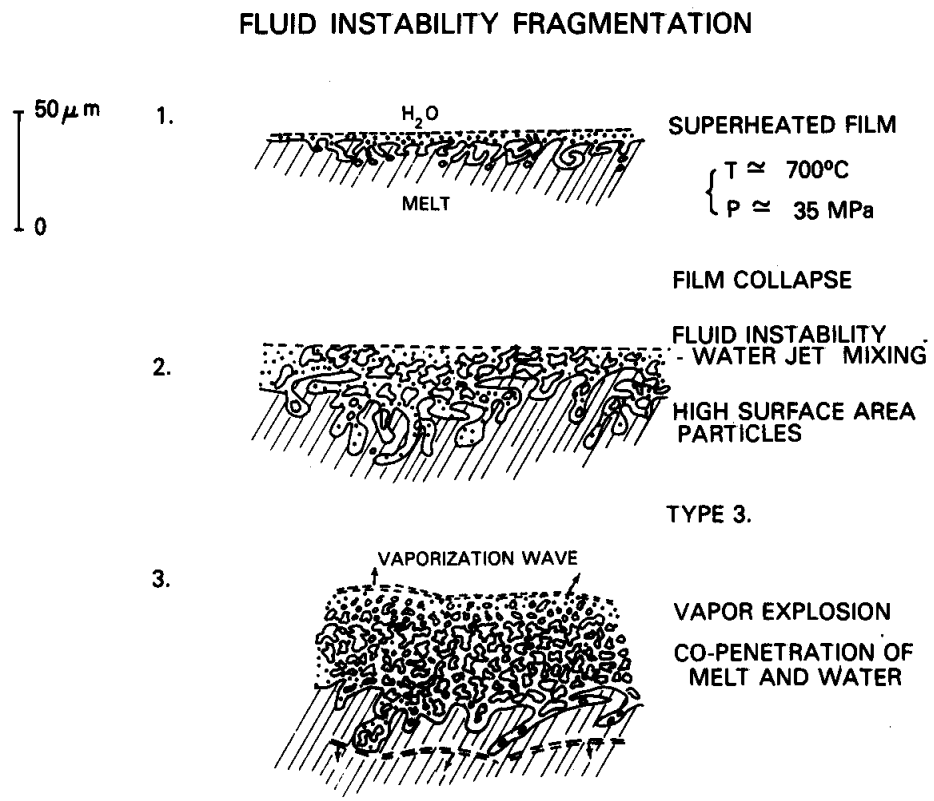

Fig. 20 Fluid instabilities can form at the contact of water with melt. These instabilities are of a Taylor type, Rayleigh-Taylor and Kelvin-Helmholtz type, or axisymmetric film collapse that causes water jets to penetrate the melt. The result is high surface-area fragmentation, rapid heat exchange, followed by vapor explosion. The explosion then generates new contact areas and/or a shock wave that fragments more melt and acts as a detonation wave. This process requires abundant water to be present.

as shown in Fig. 22. A compressive pressure wave propagating into a melt may reflect off physical boundaries due to vent geometry or density differences. Once the pressure wave reflects, it becomes negative (tensile stress) and cavitation proceeds behind the wave by formation of vesicles of exsolving melt volatiles (Corradini, 1981a). In this manner, vesiculation waves form and, if the volatile content is great enough, may cause initial fragmentation of the melt.

The fact that Types 3 and 4 pyroclasts are typically much finer grained than are Types 1 and 2 suggests that they result from higher explosion efficiencies. It follows that fragmentation due to fluid instabilities results in more complete mixing of melt and water with higher heat-transfer rates. Thus, the fine ash fraction (<63 μm diameter) indicates strong water interaction. This feature is illustrated by grain-shape correlation with deposit type. Phreatic explosion breccias, ash falls, and planar surge deposits show mostly Type 1 pyroclasts whereas sandwave and massive surge beds, accretionary lapilli beds, and vesiculated tuffs have a strong contribution of Types 3 and 4.

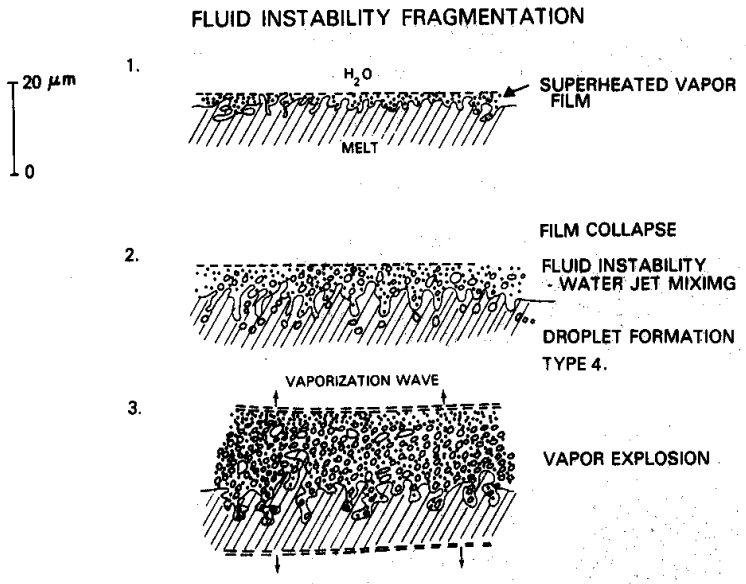

Fig. 21 Fluid instabilities will form spherical or drop-like shapes of melt if viscosity is low and surface tension affects are strong.

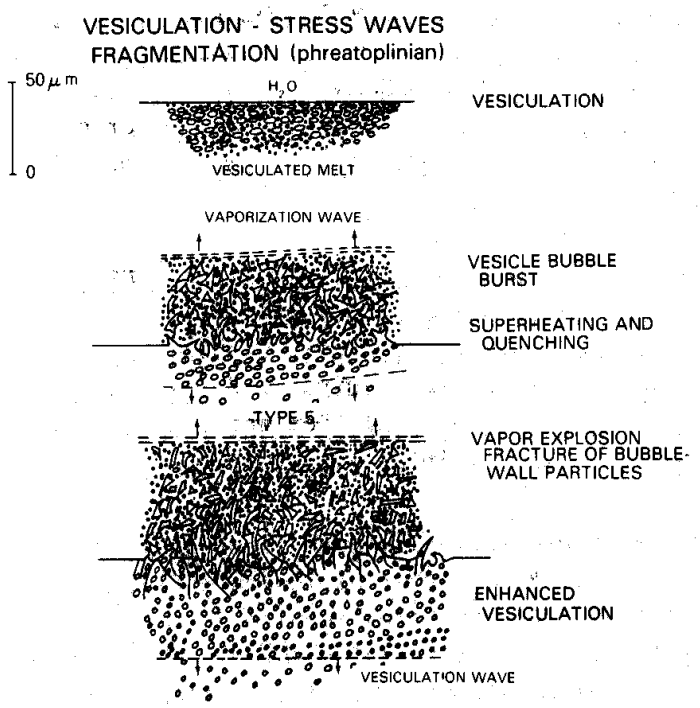

Fig. 22 Phreatoplinian fragmentation occurs when stress waves fracture bubble-wall shards formed by vesicle bubble burst. This requires contact of a vesiculating, ash-producing melt with external water during eruption and results in production of fine ash consisting of tiny plate-like forms.

CONCLUSIONS

The ash formation mechanisms discussed in this paper have both a theoretical and an experimental basis in the wealth of literature on FCIs. Comparison of ash debris from experiments that model hydrovolcanic explosions with natural samples has allowed development of several theoretical models of hydrovolcanic explosions. Although there are physical limitations to comparison of man-made metallic melts with magma, experiments demonstrate that the fragmentation mechanisms are basically the same for a wide range of melt compositions.

Shapes of experimentally produced ash particles are characterized as blocky and equant, spherical and drop-like, mossy aggregates, and the plate-like broken bubble walls. These shapes, as well as their sizes, show a strong resemblance to those of ash produced by hydrovolcanic eruptions. Comparison of volcanic ash shapes and sizes to those of artificial ash gives insight into the hydrovolcanic fragmentation mechanism.

Since rapid vaporization of water is the driving mechanism of hydrovolcanic explosions, study of the pyroclastic material generated provides information on the efficiency of the heat-transfer process. Heat transfer is dominantly conductive and requires large surface areas to reach explosive rates. Size studies of experimental debris show decreasing grain size with increasing explosive efficiency. The maximum size limit of experimental explosion debris is 2 to 3 mm with non-explosive debris being coarser. The lower boundary of size is in the submicron range. Similarly, explosive hydrovolcanic debris shows median grain sizes less than 1 or 2 mm. Size distributions do not appear to depend upon ejected volumes, but depend upon the fragmentation mechanism that occurs on a millimeter and smaller scale. For this reason, scaling is not critical when comparing experimental debris to volcanic ash.

The explosive contact of water with melt begins with the formation and collapse of steam films on the melt surface. This process is cyclic on a micro- or millisecond time scale and results in the generation of fluid instabilities at the contact, water jet penetration of the melt, and stress waves propagating into the melt. These mechanisms fragment the melt thereby increasing surface area and heat-transfer rates. Critical to the vaporization of water are the effects of superheating and detonation waves. Superheating is a process involving non-equilibrium heat transfer and homogeneous nucleation causing instantaneous vaporization. It is still poorly understood but it results in explosive efficiencies several orders of magnitude higher than those of normal boiling processes. Detonation waves are shock waves that propagate through the melt causing fragmentation of the melt and mixing with water by fluid instabilities and vapor film collapse. These waves are sensitive to the system size and permit interaction of large volumes of melt and water in a short time span.

Various debris shapes produced in melt-water interactions reflect fragmentation by brittle failure due to stress waves and viscous melt-water mixing by fluid instabilities. The latter of these two fragmentation mechanisms

appears to be the result of the most efficient explosive interactions. Hence, the production of fine-grained debris with high surface area and fluid shapes is predicted for highly explosive eruptions of fluid basalt. However, melt viscosity and strength strongly affects the tendency for development of instabilities. Therefore, brittle fragmentation dominates for intermediate and silicic melts.

Future development of a quantitative model of hydrovolcanic pyroclast formation could approach the problem of the actual amounts of external water and magma involved in explosive heat exchange during eruption. This empirical value, calculated for experiments by Corradini (1981a), may be quantitatively correlated to rates of ash production and emplacement mode. Also of importance is the partitioning of vaporization energy into fragmentation and ejection modes. These and other quantitative treatments will be the subject of future studies.

ACKNOWLEDGEMENTS

Robert McQueen provided constant support for several years in design and implementation of experiments. His scientific support and interest have made this work possible. The initial SEM work on experimental debris was completed with the help of Mike Sheridan and Rosanna DeRosa. Their ideas and encouragement are greatly appreciated. Grant Heiken provided many stimulating discussions on ash formation. Lloyd Nelson and others at Sandia National Laboratories provided encouragement as well as expert advice on FCI theory. Robert Raymond and Ronald Gooley provided technical assistance for the high resolution microscopy. I thank George Walker, Aaron Waters, and Grant Heiken for their helpful reviews of this manuscript. NASA grants NSG-7642 and NAWG-245 and funds from the Los Alamos Institutional Supporting Research and Development supplied partial support for this work.

REFERENCES

Apfel, R. E., 1972. Water superheated to 279.5°C at atmospheric pressure. Nature, 238: 63-64.

Bennett, F. D., 1974. On volcanic ash formation. Amer. J. Sci., 274: 648-661.

Berenson, P. J., 1961. Film boiling heat transfer from a horizontal surface. J. Heat Trans., August: 351-356.

Board, S. J. and Hall, R. W., 1975. Thermal explosions at molten tin/water interfaces. In: J. R. Okendon and W. R. Hodgkins (Editors), Moving Boundary Problems in Heat Flow Diffusion. Clarendon Press, Oxford, pp. 259-269.

Board, S. J., Hall, R. W. and Hall, R. S., 1975. Detonation of fuel coolant explosions. Nature, 254: 319-321.

Board, S. J., Farmer, C. L. and Poole, D. H., 1974. Fragmentation in thermal explosions. Inst. J. Heat Mass Trans., 17: 331-339.

Buchanan, D. J., 1974. A model for fuel-coolant interactions. J. Phys. D: Appl. Phys., 7: 1441-1457.

Buchanan, D. J. and Dullforce, T. A., 1973. Mechanism for vapor explosions. Nature, 245: 32-34.

Buxton, L. D. and Benedict, W. B., 1979. Steam explosion efficiency studies. Sandia National Laboratories, SAND79-1399, NUREG/CR-0947, pp. 1-62.

Carlisle, D., 1963. Pillow breccias and their aquagene tuffs, Quadra Island, British Columbia. J. Geol., 71: 48-71.

Colgate, S. A. and Sigurgeirsson, T., 1973. Dynamic mixing of water and lava. Nature, 244: 552-555.

Corradini, M. L., 1981a. Analysis and modelling of steam explosion experiments. Sandia National Laboratories, SAND80-2131, NUREG/CR-2072, pp. 1-114.

Corradini, M. L., 1981b. Phenomenological modelling of the triggering phase of small-scale steam explosion experiments. Nucl. Sci. Eng., 78: 154-170.

Drumheller, D. S., 1979. The initiation of melt fragmentation in fuel-coolant interactions. Nucl. Sci. Eng., 72: 347-356.

Dullforce, T. A., Buchanan, D. J. and Peckover, R. S., 1976. Self triggering of small-scale fuel-coolant interactions: I experiments. J. Phys. D.: Appl. Phys., 9: 1295-1303.

Fisher, R. V. and Waters, A. C., 1969. Bedforms in base surge deposits: Lunar implications. Sci., 165: 1349-1352.

Fisher, R. V. and Waters, A. C., 1970. Base surge bedforms in maar volcanoes. Amer. J. Sci., 268: 157-180.

Fröhlich, G., Müller, G. and Unger, G., 1976. Experiments with water and hot melts of lead. J. Non-Equilib. Thermodyn., 1: 91-103.

Fuller, R. E., 1931. The aqueous chilling of basaltic lava on the Columbia River Plateau. Amer. J. Sci., 21: 281-300.

Galloway, W. J., 1954. An experimental study of acoustically induced cavitation in liquids. J. Acoust. Soc. Amer., 26: 849-857.

Heiken, G. H., 1971. Tuff rings: examples from the Fort Rock-Christmas Lake Valley, south-central Oregon. J. Geophys. Res., 76: 5615-1626.

Heiken, G. H., 1972. Morphology and petrography of volcanic ashes. Geol. Soc. Amer. Bull., 83: 1961-1988.

Heiken, G. H., 1974. An atlas of volcanic ash. Smithsonian Contrib. Earth Science, 12: 1-101.

Honnorez, J. and Kirst, P., 1975. Submarine basaltic volcanism: morphometric parameters for discriminating hyaloclastites from hyalotuffs. Bull. Volcanol., 32: 441-465.

Jaggar, T. A., 1949. Steam blast volcanic eruptions. Hawaiian Volcano Observatory, 4th Spec. Report, pp. 1-137.

Kazimi, M. S., 1976. Acoustic cavitation as a mechanism of fragmentation of molten droplets in coolant liquids. MIT Report, CO-2781-6TR.

Lipsett, S. G., 1966. Explosions from molten materials and water. Fire Tech., May: 118-126.

McBirney, A. R., 1963. Factors governing the nature of submarine volcanism. Bull. Volcanol., 26: 455-469.

McBirney, A. R. and Murase, T., 1970. Factors governing the formation of pyroclastic rocks. Bull. Volcanol, 34: 372-384.

Moore, J.G., 1967. Base surge in recent volcanic eruptions. Bull. Volcanol., 30: 337-363.

Nelson, L. S. and Duda, P. M., 1981. Steam explosion experiments with single drops of CO_2 laser-melted iron oxide. Trans. Amer. Nucl. Soc., 38: 453-454.

Nelson, L.S., Buxton, L.D. and Planner, H.N., 1980. Steam explosion triggering phenomena, Part 2: Corium-A and Corium-E and oxides of iron and cobalt studied with a floodable arc-melting apparatus. Sandia Laboratories, SAND79-0260, NUREG/CR-0633.

Nelson, L. S. and Buxton, L. D., 1978. Steam explosion triggering phenomena: stainless steel and corium-E similants studied with a floodable arc melting apparatus. Sandia Laboratories, SAND77-0998, NUREG/CR-0122.

Peacock, M. A., 1926. The basic tuffs. In: G. W. Tyrell and M. A. Peacock (Editors), The petrology of Iceland. Royal Soc. Edinburgh Trans., 45: 51-76.

Peckover, R. S., Buchanan, D. J. and Ashby, D. E. T. F., 1973a. Fuel-coolant interactions in submarine volcanism. Nature, 245: 307-308.

Peckover, R. S., Buchanan, D. J. and Ashby, D. E. T. F., 1973b. Fuel-coolant interactions in submarine volcanism. Culham Laboratory Publ., Abingdon, pp. 1-348.

Reid, R. C., 1976. Superheated liquids. Amer. Sci., 64: 146-156.

Sandia Laboratories, 1975. Core-meltdown experimental review. SAND74-0382, pp. 1-472.

Self, S. and Sparks, R. S. J., 1978. Characteristics of widespread pyroclastic deposits formed by the interaction of silicic magma and water. Bull. Volcanol., 41-3: 196-212.

Sheridan, M. F., Barberi, F., Rosi, M., and Santacroce, R., 1981. A model for Plinian eruptions of Vesuvius. Nature, 289: 282-285.

Sheridan, M. F. and Marshall, J. R., 1982. SEM examination of pyroclastic materials: basic considerations. SEM Inc., (in press).

Sheridan, M. F. and Updike, R., 1975. Sugarloaf Mountain tephra - a Pleistocene rhyolite deposit of base-surge origin. Geol. Soc. Amer. Bull., 86: 571-581.

Sheridan, M. F. and Wohletz, K. H., 1981. Hydrovolcanic explosions, the systematics of water-pyroclast equilibration. Science, 212: 1387-1389.

Sparks, R. S. J., 1978. The dynamics of bubble formation and growth in magmas: a review and analysis. J. Volcanol. Geotherm. Res., 3: 1-37.

Tazieff, H., 1968. Sur le mécanisme des eruptions basaltiques sous-marines a faibles profundeurs et la genese d'hyaloclastites associeés. Geol. Rund., 57: 955-966.

Theofonus, T. G., 1979. Fuel-coolant interactions and hydrodynamic fragmentation. Proceedings of the Fast Reactor Safety Meeting, Seattle, Washington.

Thorarinsson, S., 1966. Surtsey the new island in the North Atlantic. Almenna Bokafelagid, Reykjavik, pp. 1-47.

Verhoogen, J., 1951. Mechanics of ash formation. Amer. J. Sci., 249: 729-739.

von Waltershausen, W. S., 1853. Uber die vulkanischen gesteine in Sizilien und Island und ihre submarine umbildung. Gottingen.

Walker, G. P. L., 1971. Grain-size characteristics of pyroclastic deposits. J. Geol., 79: 696-714.

Walker, G. P. L., 1973. Explosive volcanic eruptions - a new classification scheme. Sond. Geol. Rund., 62: 431-446.

Walker, G. P. L. and Croasdale, R., 1971. Characteristics of some basaltic pyroclastics. Bull. Volcanol., 35: 305-317.

Weast, L. C., 1977. CRC handbook of chemistry and physics 58th. CRC Press Inc. Cleveland, Ohio.

Witte, L. C., Cox, J. E. and Bouvier, J. E., 1970. The vapor explosion. J. Metals, 22: 39-44.

Wohletz, K. H., 1980. Explosive hydromagmatic volcanism. Ph.D. Thesis, Arizona State University, Tempe, Arizona, pp. 1-303.

Wohletz, K. H. and Krinsley, D. H., 1982. Scanning electron microscopic analysis of basaltic hydromagmatic ash. In: B. Whaley and D. Krinsley (Editors), Scanning Electron Microscopy in Geology. Geo. Abstracts, Inc., Norwich, England.

Wohletz, K. H. and McQueen, R. G., 1981. Experimental hydromagmatic volcanism. Amer. Geophys. Union Trans., EOS, 62(45): 1085.

Wohletz, K. H. and McQueen, R. G., in press. Experimental studies of hydromagmatic volcanism. In: F. R. Boyd (Editor), Explosive volcanism: inception, evolution, and hazards. Studies in Geophysics, National Academy Sciences.

Wohletz, K. H. and Sheridan, M. F., 1979. A model of pyroclastic surge. In: C.E. Chapin and W.E. Elston (Editors), Ash-flow Tuffs. Geol. Soc. Amer. Spec. Paper, 180: 177-193.

Wohletz, K. H. and Sheridan, M. F., 1982. Hydrovolcanic explosions II: evolution of tuff cones and tuff rings. Amer. J. Sci., (in press).

+